Revue Internationale
de Géomatique

Tech Science Press

https://doi.org/10.32604/rig.2026.089924

ARTICLE

Non-Stationary Wind Characteristics in Coastal Wind Farms during Typhoons Based on BFAST and Hurst Exponent: A Case Study of Lekima

Liyuan Deng[1], Aodi Fu[2,*], Jing Tan[3], Bing Bing[4], Linzi Wang[1], Haibo Shen[1] and Huijun Wu[1]

[1]Power Dispatching and Control Center of China Southern Power Grid, Guangzhou, China
[2]School of Renewable Energy, Hohai University, Changzhou, China
[3]School of Management, Shanghai University of Engineering Science, Shanghai, China
[4]Meteorological Bureau of Zhaoyuan City, Zhaoyuan, China

*Corresponding Author: Aodi Fu. Email: 250215020001@hhu.edu.cn

Received: 01 August 2026; Accepted: 25 August 2026; Published: 25 September 2026

ABSTRACT: The non-stationarity and vertical coupling of the boundary-layer wind field during typhoon passage are key concerns for wind engineering and disaster prevention. Using hourly ERA5 reanalysis data, this study investigates the evolution of the 10 and 100 m wind fields throughout Typhoon Lekima (2019) by combining BFAST breakpoint detection, Hurst exponent analysis, correlation analysis, and segmented linear fitting, together with near-surface temperature, 850 hPa temperature, and mean sea level pressure fields. BFAST detected a structural breakpoint at all 525 grid cells, with breakpoint timing progressing along the storm track (median 26 h at 10 m and 33 h at 100 m) and magnitudes positive in the northeast and negative in the southwest; at the tower, breakpoints at both heights occurred synchronously at 43 h, with a larger jump at 100 m (+2.20 m s^{-1}) than at 10 m (+1.34 m s^{-1}). The two heights remained strongly correlated (domain-mean r = 0.991) with a nearly constant speed ratio of ~1.45 consistent with the logarithmic profile, while wind-direction correlation degraded only within the inner-core region (minimum r = 0.49). The wind-speed Hurst exponent fell from ~1.04 to 0.84 after center passage, whereas the wind-direction exponent rose from 0.88 to 0.91, indicating that turbulent energy injection disrupted wind-speed persistence while wind direction stabilized under the reorganized flow. The pre-to-post transition in non-stationarity is attributed to a shift in boundary-layer forcing from large-scale baroclinic driving to localized thermal perturbations, with the loss of directional coherence in the pressure gradient field weakening the long-range dependence of the wind field.

KEYWORDS: Typhoon Lekima; boundary layer wind field; BFAST breakpoint detection; Hurst exponent; non-stationarity; vertical correlation

1 Introduction

The development of clean energy is an important part of China's "dual carbon" goal. As a key component of clean energy, wind energy is of great significance for the transformation of the energy structure and the response to climate change [1]. As of 2022, China's installed wind power capacity was approximately 370 million kW. While the wind power industry is booming, it also faces various crises and challenges. China's coastal areas are attacked by typhoons of varying intensity every year, and typhoon characteristic parameters serve as important considerations for the siting of wind farms and the design of wind turbines. Therefore, analyzing the wind variation characteristics of wind farms during typhoons is crucial for the safe and stable operation of wind turbines [2].

Copyright © 2026 The Authors. Published by Tech Science Press. This work is licensed under a Creative Commons Attribution 4.0 International License, which permits unrestricted use, distribution, and reproduction in any medium, provided the original work is properly cited.

Existing research on typhoon wind characteristics mostly focuses on wind speed, wind direction, wind attack angle, turbulence intensity, and related parameters. Methods such as linear trend fitting and qualitative analysis are commonly used to characterize their evolution [3]. However, under the influence of a typhoon, wind speed and wind direction are highly non-stationary, exhibiting abrupt structural changes (e.g., sudden acceleration or directional shifts during the passage of the storm center) as well as long-range dependence (memory). Traditional methods that assume stationarity are therefore insufficient: linear trend fitting can describe only a single monotonic trend and cannot detect multiple structural change points, while conventional statistical descriptors (e.g., means and standard deviations) cannot reveal the memory or persistence of the wind field [4]. Consequently, nonlinear and non-stationary analysis methods are required to better characterize the wind field evolution during typhoon events [5].

A variety of nonlinear methods have been developed to detect non-stationarity and nonlinearity in time series, including wavelet analysis, empirical mode decomposition (EMD) [6], DBEST [7], and BFAST. Based on daily sounding wind data over Wuhan from 1958 to 2013, Chen and Meng analyzed the non-stationary characteristics of annual, seasonal, and monthly mean wind speeds using wavelet analysis and the Yamamoto mutation test [8]; such long-time-scale wind variation characteristics can provide early technical support for regional wind-resource assessment and wind-farm siting and design. More recently, attention has shifted toward short-term wind characteristics. EMD is an adaptive signal-processing method that explores local time characteristics and can handle non-stationary trends; however, when all extreme points are used, noise increases the EMD error and distorts the prediction results [9]. BFAST can identify long-term trends and breakpoint changes in time series and can explicitly separate periodic components [10]. For example, He et al. used BFAST to analyze the non-stationary characteristics and spatial distribution of drought, providing a basis for disaster-reduction work in Xinjiang [11].

Complementary to breakpoint-based methods, the Hurst exponent quantifies the long-range dependence (memory) of a time series, yielding a scalar measure of persistence or anti-persistence [12]. Whereas BFAST characterizes the location, magnitude, and trends of structural change points, the Hurst exponent captures the temporal memory of the sequence before and after such changes. These two approaches are therefore complementary: BFAST reveals where and how the wind-field regime shifts, while the Hurst exponent reveals whether the wind field retains long-range memory or degrades into short-term fluctuations [13]. Although time series breakpoint detection and persistence analysis have been applied separately in previous meteorological studies, their combined application to the typhoon boundary layer remains limited. The specific scientific novelty of this study lies in two aspects: (i) it provides a new spatial-scale assessment of the synchronicity of structural changes in the 10–100 m boundary-layer wind field, revealing whether the timing and magnitude of breakpoints are vertically coherent; and (ii) it offers new insights into the relationship between changes in wind speed persistence (quantified by the Hurst exponent) and the dynamic forcing before and after typhoon passage.

This study is based on ERA5 data from the region affected by Typhoon Lekima. The BFAST method and Hurst exponent analysis were employed to investigate the non-stationary characteristics of wind speed and wind direction at 10 and 100 m heights during the typhoon impact period. Furthermore, correlation analysis was conducted using mesoscale meteorological variables to explore the mechanisms influencing wind-field non-stationarity. Specifically, this study aims to address the following questions:

(1) Temporal change-point detection and segmented trend analysis of wind field sequences using the BFAST method;

(2) Long-range dependence characteristics of wind speed sequences during typhoon-affected periods;

(3) Spatial heterogeneity and mesoscale meteorological controls of wind field non-stationarity.

BFAST method combined with Hurst exponent is used to analyze the change characteristics of wind speed and direction in wind farms, providing method support for the study of wind sequence characteristics and theoretical guidance for the design of wind turbines.

2 Method

2.1 Break Detection in the Seasonal and Trend (BFAST)

BFAST decomposes a time series into seasonal, trend, and residual components and detects change points in the trend and seasonal parts, as in Eq. (1). The method has been applied to long-term trend and breakpoint detection, and it reports the fitted trend together with its confidence interval and the locations of the breakpoints [7,9]. In this study we used the BFAST01 package in R—a variant of BFAST that fits at most one breakpoint—to examine the wind speed and wind direction series at the four tower heights and to characterize their non-stationary behavior during the typhoon. The model is written as:

$$Y_t = S_t + T_t + e_t \quad (t = 1, 2, 3, \cdots, n) \tag{1}$$

where Y_t is the observed value at time t, S_t is the seasonal component capturing the annual cycle, T_t is the long-term trend that may contain abrupt changes, and e_t is the residual, that is, the unexplained variation left after removing the trend and seasonal components. Because the wind speed and wind direction series change on short timescales during a typhoon, only the trend component and the detected breakpoints are considered in this study; the seasonal and periodic components are not discussed.

The BFAST analysis was performed with the "bfast" package in R (version 4.3.1). Because this study focuses on the short-term wind-field variation during the typhoon rather than long-term seasonal changes, the seasonal component was omitted from the decomposition, and only the trend component and its structural changes were analyzed.

Single-breakpoint detection was carried out with the bfast01 function, which fits at most one breakpoint, consistent with the aim of identifying the primary regime shift associated with the passage of Typhoon Lekima. The minimum segment size (the h parameter, expressed as a fraction of the series length) was chosen so that enough observations remained on each side of the breakpoint for reliable trend estimation. A breakpoint was retained as significant when its confidence level exceeded 95% ($p < 0.05$).

After a breakpoint was identified, segmented linear regression was applied to characterize the pre- and post-breakpoint trends, and the timing and magnitude of the detected changes were then used to describe the non-stationary behavior of wind speed and wind direction during the typhoon.

2.2 Hurst Stationarity Analysis of Time Series

(1) The Hurst exponent was calculated using the rescaled range (R/S) method [14]. For a time series $P(t)$ with length N:

$$P(t) \quad t = 1, 2 \cdots, N \tag{2}$$

the sequence is divided into A consecutive non-overlapping subintervals I_a with equal length n, where:

$$N = A \times N \tag{3}$$

Each subinterval is expressed as:

$$\mathrm{I_a} = \{P_{k,a} | k = 1, 2, \cdots, n\}, (a = 1, 2, \cdots, A) \tag{4}$$

For each subinterval, the mean value is calculated as:

$$e_a = \frac{1}{n}\sum_{k=1}^{n} P_{k,a} \tag{5}$$

(2) The standard deviation S_a, cumulative deviation $X_{k,a}$, and range R_a are calculated as:

$$S_a = \sqrt{\frac{1}{n}\sum_{k=1}^{n}(P_{k,a} - e_a)^2} \tag{6}$$

$$x_{k,a} = \sum_{j=1}^{k}\left(P_{j,a} - e_a\right) \tag{7}$$

$$R_a = \max_{1\le k\le n}\left(x_{k,a}\right) - \min_{1\le k\le n}\left(x_{k,a}\right) \tag{8}$$

(3) The rescaled range statistic for each subinterval is:

$$(R/S)_n = \frac{1}{A}\sum_{a=1}^{A}\left(\frac{R_a}{S_a}\right) \tag{9}$$

(4) By changing the subinterval length n, the relationship between $(R/S)_n$ and n follows:

$$\lg\left(\left(\frac{R}{S}\right)_n\right) = lgC + Hlgn \tag{10}$$

where H is the Hurst exponent obtained from the slope of the least-square linear regression.

The Hurst exponent characterizes the long-range dependence of time series. When $0 < H < 0.5$, the sequence exhibits anti-persistent behavior. When $H \approx 0.5$, the sequence behaves as an uncorrelated random process similar to white noise. When $0.5 < H < 1$, the sequence exhibits persistent long-range correlation.

It should be noted that the classical Hurst exponent theoretically ranges from 0 to 1 for stationary stochastic processes. However, in practical applications, especially for short-term and strongly non-stationary environmental time series, the estimated Hurst exponent may occasionally exceed 1 due to the influence of deterministic trends, finite sample length, and abrupt structural changes within the sequence.

In this study, the wind speed and wind direction sequences were obtained during the passage of Typhoon Lekima, which involved rapid intensification, peak wind conditions, and subsequent weakening processes. These strong non-stationary variations may introduce additional trend components into the R/S calculation, resulting in Hurst exponent values slightly higher than 1. Therefore, the Hurst exponent values greater than 1 in this study are interpreted as indicating extremely strong persistence and dominant trend-driven behavior rather than as a violation of the theoretical definition of the Hurst exponent.

3 Overview of Typhoon Likima and Its Data Sources

3.1 Overview of Typhoon Lekima

The track of the typhoon near-center (the near-center path of the typhoon) is shown in Fig. 1. On 4 August 2019, Typhoon 201909 “Lekima” strengthened into a tropical storm in the northwest Pacific Ocean. From August 4 to August 10, it moved rapidly to the northwest, crossed the East China Sea, and made landfall in Wenling City, Zhejiang Province, China as a super typhoon on August 10, with a central wind speed of 52 m/s. Then it went all the way north and passed Dafeng District, Yancheng City, Jiangsu Province at 7:00 on August 11. It finally disappeared at 11:00 on 13 August 2019 in Bohai Sea, China.

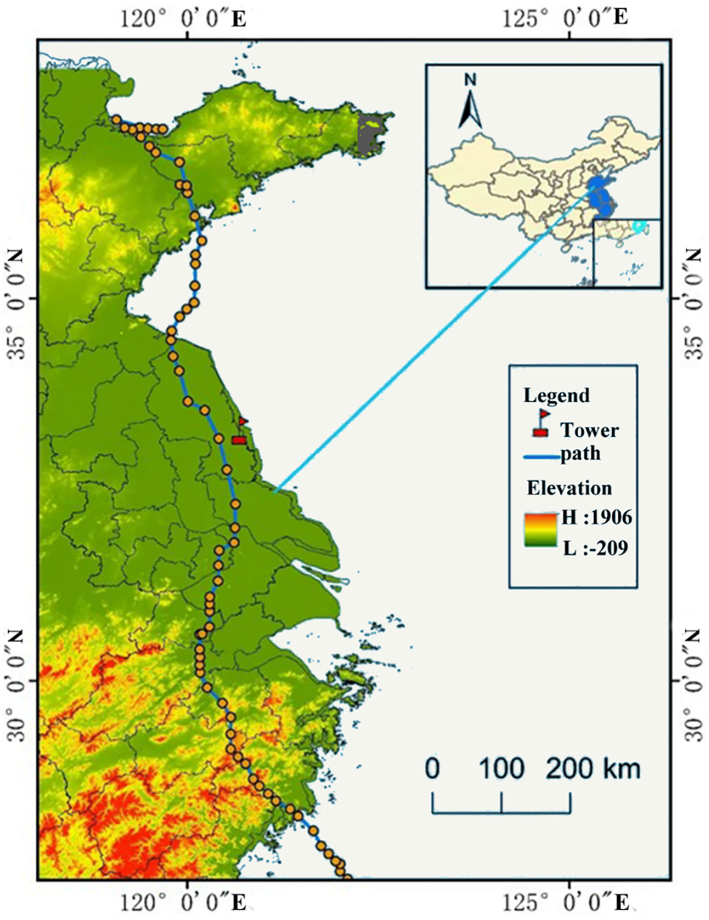


Figure 1: Overview of Typhoon Lekima.

3.2 Study Area and Spatial Data

The study area covers the coastal region affected by Typhoon Lekima (2019), with a spatial extent of 117° E–123° E and 30° N–35° N. This region is located in the eastern coastal area of China and includes the main influence area of Typhoon Lekima during its northward movement after landfall. The region is characterized by complex land–sea interaction processes and strong atmospheric variability, making it an ideal area for investigating the short-term non-stationary characteristics of coastal wind fields under typhoon conditions.

In this study, ERA5 reanalysis data were used as the primary meteorological dataset to characterize the spatial and temporal evolution of the wind field during the typhoon event. The ERA5 dataset provides hourly atmospheric variables with a horizontal spatial resolution of 0.25° × 0.25°. Within the selected domain (117° E–123° E, 30° N–35° N), a total of 525 grid points were included, consisting of 21 latitude grids and 25 longitude grids. These spatial grids were used to analyze the spatial distribution characteristics of wind-field breakpoint changes, Hurst exponent variations, and the responses of wind-field non-stationarity to mesoscale meteorological forcing.

The representative wind farm location in Dafeng District, Yancheng City, Jiangsu Province (approximately 120.7° E, 33.3° N) was selected as a reference point for detailed temporal analysis. It should be noted that this study does not use *in-situ* observations from the wind tower; instead, the ERA5 grid data corresponding to this location were extracted to represent the local wind-field characteristics. The selected

location is situated within the influence range of Typhoon Lekima during its passage, allowing the evolution of wind speed and wind direction before, during, and after the typhoon impact to be investigated.

3.3 Data Source

To characterize the temporal variability of the typhoon wind field and the tower-site wind field from 00:00 UTC on 8 August 2019 to 23:00 UTC on 13 August 2019 and to investigate the atmospheric forcing mechanisms associated with typhoon-induced wind variability, mesoscale meteorological variables were incorporated into the analysis. These variables included mean sea level pressure (MSLP), surface pressure, air temperature at 850 hPa, 2 m air temperature, 10 m zonal wind component (u10), 10 m meridional wind component (v10), 100 m zonal wind component (u100), and 100 m meridional wind component (v100). All meteorological variables were obtained from the Climate Data Store (CDS, https://cds.climate.copernicus.eu/datasets) based on the ERA5 reanalysis dataset, which provides hourly atmospheric data at a spatial resolution of 0.25° × 0.25°.

The horizontal wind fields at 10 and 100 m were computed by combining the zonal and meridional wind components:

$$U = \sqrt{u^2 + v^2} \tag{11}$$

where U represents the resultant horizontal wind speed, and u and v denote the zonal and meridional wind components, respectively. The reconstructed 10 m wind field was used to characterize near-surface atmospheric circulation, while the 100 m wind field was selected to represent the lower atmospheric boundary-layer conditions close to typical wind turbine hub heights. These multi-scale meteorological variables were subsequently used to explore the spatial response of wind field non-stationarity to mesoscale atmospheric forcing during typhoon events.

4 Results and Analysis

4.1 Characteristic Analysis of Wind Speed and Direction Change

Analysis of the wind speed time series reveals that Typhoon Lekima exerted a prolonged influence on both the broader wind field and the tower site, with wind speed and direction exhibiting dramatic variations throughout the typhoon passage. In this study, the BFAST method is employed to characterize the non-stationary features of wind speed and direction during Typhoon Lekima.

Fig. 2 showed that BFAST Breakpoint Spatial Distribution. At a 100% detection rate, BFAST single-breakpoint detection identified a structural change point, indicating that the entire domain underwent a systematic regime shift during Typhoon Lekima's passage. The spatial distribution of breakpoint timing at the 10 m level (Fig. 2a) exhibited a median of 26 h and a mean of 32.5 h, with earlier breakpoints (21–30 h) concentrated in the southeastern quadrant along the storm track approach and progressively later breakpoints (50–75 h) in the northwestern periphery. The 100 m breakpoint timing (Fig. 2b) showed a broadly similar spatial pattern but with a slightly later mean of 35.4 h (median 33 h), suggesting that the structural transition at the upper observational level lagged behind that at 10 m, a phenomenon that may be attributable to the vertical propagation time of momentum adjustments through the Ekman layer. The breakpoint magnitude maps (Fig. 2c,d) revealed notable spatial asymmetry. Positive magnitudes (post-break wind speed exceeding pre-break values) were predominantly observed in a band aligned with and to the northeast of the storm track, with maximum increases reaching 6.10 m/s at 10 m and 7.85 m/s at 100 m. Negative magnitudes (wind speed decline following the breakpoint) occurred primarily in the southwestern sector, possibly reflecting the spatial inhomogeneity of the typhoon's wind field evolution. The 100 m

magnitude field (mean 1.79 m/s) consistently exceeded that of 10 m (mean 1.35 m/s), suggesting stronger sensitivity of the upper boundary layer to the synoptic-scale forcing transition.

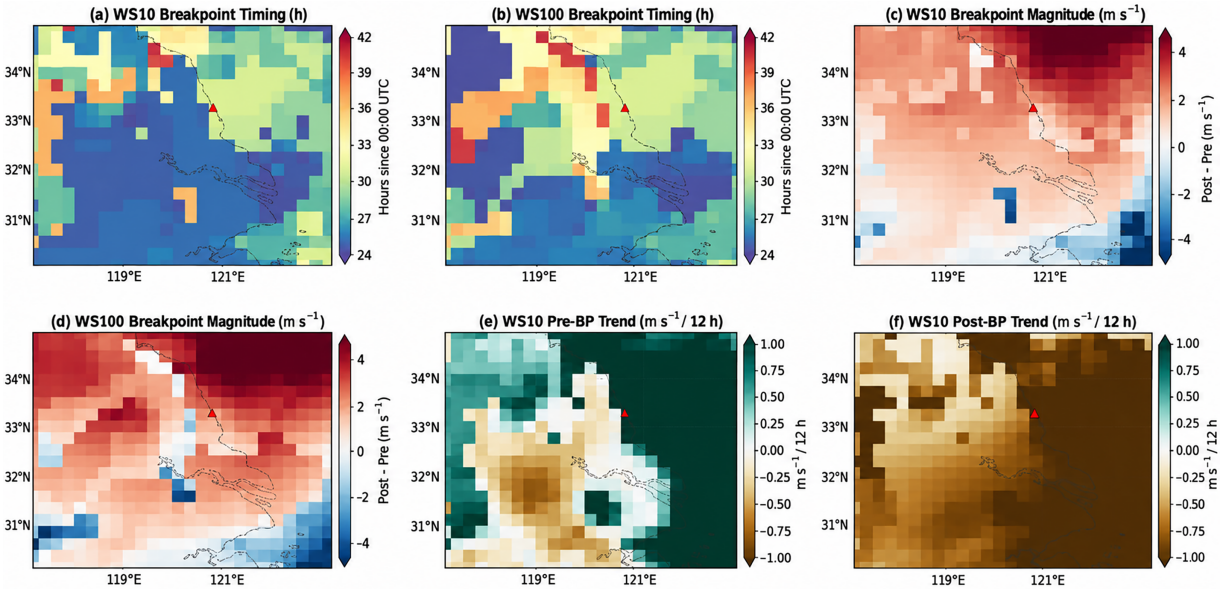


Figure 2: BFAST single-breakpoint detection: 10 and 100 m wind speed Typhoon "Lekima". (**a**) WS10 breakpoint timing (h), (**b**) WS100 breakpoint timing (h), (**c**) WS10 breakpcint magnitude (m/s), (**d**) WS100 breakpoint magnitude (m/s), (**e**) WS10 Pre-BP trend (m s/12 h), (**f**) WS10 Post-4BP trend (m/s/12 h).

The pre- and post-breakpoint trend fields at 10 m (Fig. 2e,f) characterized the temporal asymmetry of the regime shift. Pre-break trends were predominantly positive (mean +0.06 m/s/h), corresponding to the wind acceleration phase during the typhoon's approach. Post-break trends reversed sign across most of the domain (mean −0.08 m/s/h), suggesting systematic wind decay following the structural transition. However, localized patches of continued positive post-break trends in the northeastern sector suggested sustained wind enhancement in the typhoon's right-front quadrant, broadly consistent with the asymmetric boundary layer dynamics of translating tropical cyclones.

In Fig. 3, BFAST single-breakpoint detection and segmented linear fitting of wind speed time series at the tower site (120.7° E, 33.3° N). The BFAST-detected breakpoint at the tower location occurred at 43 h (03:00 on August 10), synchronously at both the 10 and 100 m levels. The pre-break segment exhibited a positive linear trend, with wind speed increasing at 0.099 and 0.144 m/s/h at 10 and 100 m, respectively. The post-break segment reversed to a negative tendency (−0.114 and −0.161 m/s/h), depicting a rise-to-decay transition in the local wind field.

The magnitude of the structural jump at the tower was measured at +1.34 m/s (10 m) and +2.20 m/s (100 m). The 64% larger magnitude at the upper level is dynamically consistent with the logarithmic wind profile: at a given friction velocity, the same relative change in wind speed corresponds to a larger absolute increment at greater heights where the background wind speed is higher. The nearly identical breakpoint timing at both heights further confirms that the structural change propagated coherently through the boundary layer column. Furthermore, as the maximum wind speed was observed at 03:00 on 11 August, this time was adopted as the partition point, with the preceding period designated as the pre-center-passage phase and the subsequent period designated as the post-center-passage phase, serving as the temporal framework for the subsequent analyses of wind speed and direction persistence and their influencing factors.

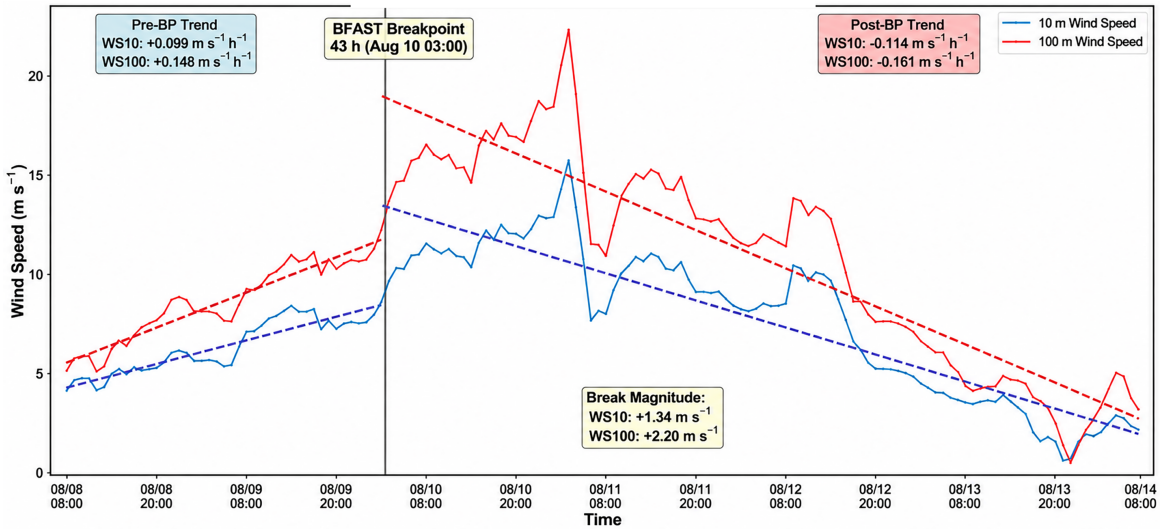


Figure 3: BFAST single-breakpoint detection at tower (120.7° E, 33.3° N) Typhoon "Lekima".

4.2 Hurst Exponent Analysis

In order to further verify and analyze the non-stationary characteristics of wind speed and wind direction time series, R/S method is used to calculate Hurst exponent to analyze the change characteristics of wind speed and wind direction time series. Figs. 4 and 5 present the spatial distributions of the Hurst exponent derived from the wind speed and wind direction time series, respectively, characterizing the long-range persistence of the wind field during Typhoon Lekima. The corresponding Hurst exponent values extracted at the tower site are summarized in Table 1. The spatial distributions of the Hurst exponent for wind speed (Fig. 4a–f in hurst_ws_spatial) and wind direction (hurst_wd_spatial) across 525 grid cells during Typhoon Lekima revealed fundamentally distinct spatiotemporal behaviors between the two wind field components.

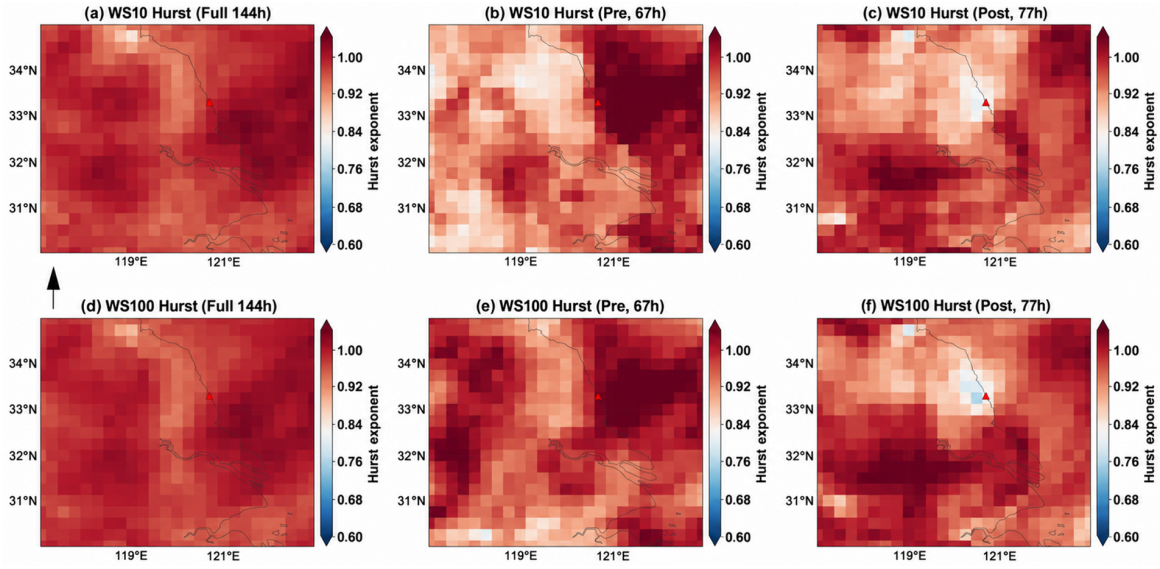


Figure 4: Hurst exponent analysis of wind speed (10 & 100 m) Typhoon "Lekima". (**a**) WS10 Hurst (Full 144 h), (**b**) WS10 Hurst (Pre, 67 h), (**c**) WS10 Hurst (Post, 77 h), (**d**) WS100 Hurst (Full 144 h), (**e**) WS100 Hurst (Pre, 67 h), (**f**) WS100 Hurst (Post, 77 h).

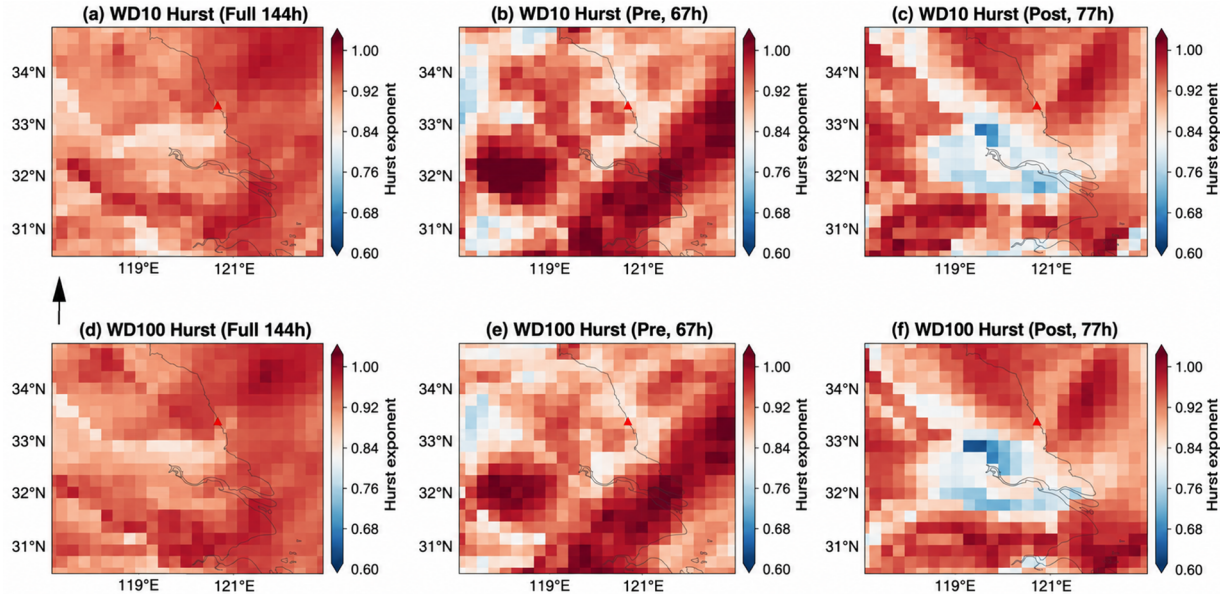


Figure 5: Hurst exponent analysis of wind direction (10 & 100 m) Typhoon "Lekima". (**a**) WD10 Hurst (Full 144 h), (**b**) WD10 Hurst (Pre, 67 h), (**c**) WD10 Hurst (Post, 77 h), (**d**) WD100 Hurst (Full 144 h), (**e**) WD100 Hurst (Pre, 67 h), (**f**) WD100 Hurst (Post, 77 h).

Table 1: Hurst exponents of wind speed and direction at the tower site.

Height	Full Period	Pre-Typhoon	Post-Typhoon	Pre to Post Change
10 m WS	1.001	1.037	0.842	−0.195
10 m WD	0.938	0.885	0.915	0.030
100 m WS	0.995	1.045	0.841	−0.204
100 m WD	0.948	0.883	0.911	0.028

For wind speed, the domain-averaged Hurst exponent over the full 144 h record was 0.988 and 0.991 at 10 and 100 m, respectively, approaching or slightly exceeding the theoretical upper bound of 1.0, indicating extremely strong persistence dominated by the deterministic evolution of the typhoon-driven wind field. The pre-typhoon segment (first 67 h) exhibited slightly lower spatial means (H = 0.954 at 10 m, 0.981 at 100 m) compared with the post-typhoon segment (H = 0.959 at 10 m, 0.971 at 100 m) at the domain level. However, the tower-scale analysis revealed a contrasting pattern: at the specific observation site, wind speed Hurst exponents decreased substantially from pre- to post-typhoon phases (10 m: 1.037 to 0.842; 100 m: 1.045 to 0.841), with the sharpest declines observed along the immediate storm track. This spatial heterogeneity—domain-mean stability masking localized persistence loss—demonstrates that typhoon-induced turbulence degradation of the long-range memory of wind speed was geographically concentrated within the inner-core impact zone rather than being a basin-wide phenomenon.

Wind direction Hurst exponents displayed markedly different characteristics. The full-period domain means (H = 0.939 at 10 m, 0.948 at 100 m) were lower than those of wind speed, and the pre-to-post transition exhibited the opposite sign of change. At the tower, tab1 showed that directional Hurst increased from 0.885 (pre) to 0.915 (post) at 10 m, and from 0.883 to 0.911 at 100 m. Spatially, the post-typhoon directional Hurst field (H = 0.916 to 0.918, domain mean) was slightly below the pre-typhoon values (H = 0.934 to 0.937), owing to scattered low-H patches in the northwestern sector where directional instability persisted

following the storm's passage. Nevertheless, the overwhelming majority of grid cells maintained H > 0.85 across both periods, confirming that wind direction sequences retained strong inertial memory throughout the typhoon lifecycle.

4.3 Spatiotemporal Correlation Analysis of Wind Fields

Figs. 6 and 7 show that the 10 and 100 m wind fields exhibited highly consistent linear coupling throughout the passage of Typhoon Lekima. Segmented analysis at the tower site, partitioned at 03:00 on 11 August, yielded pre- and post-typhoon Pearson correlation coefficients of 0.998 and 0.995 (R^2 = 0.996 and 0.991) for wind speed, with a stable speed ratio of approximately 1.47 that conformed to the logarithmic wind profile and remained invariant across the typhoon passage. Wind direction correlations exceeded 0.999 (R^2 > 0.998) in both segments, indicating negligible vertical directional shear within the 10–100 m layer. Spatial grid-based analysis over all 525 grid cells further demonstrated that the mean wind speed correlation reached 0.991 domain-wide, with only a modest reduction to 0.95 in coastal land areas attributable to enhanced surface roughness. In contrast, the degradation of wind direction correlation (minimum r = 0.49) and the elevated RMSE (maximum 20°) were spatially confined to the typhoon inner-core region, confirming that the directional mismatch between the 10 and 100 m levels induced by strong horizontal wind shear was a localized phenomenon rather than a symptom of large-scale boundary layer decoupling. Collectively, these results demonstrate that the correlation between 10 and 100 m winds within the typhoon boundary layer exhibits robust spatiotemporal stability, with only localized directional perturbations occurring in the inner-core vortex region.

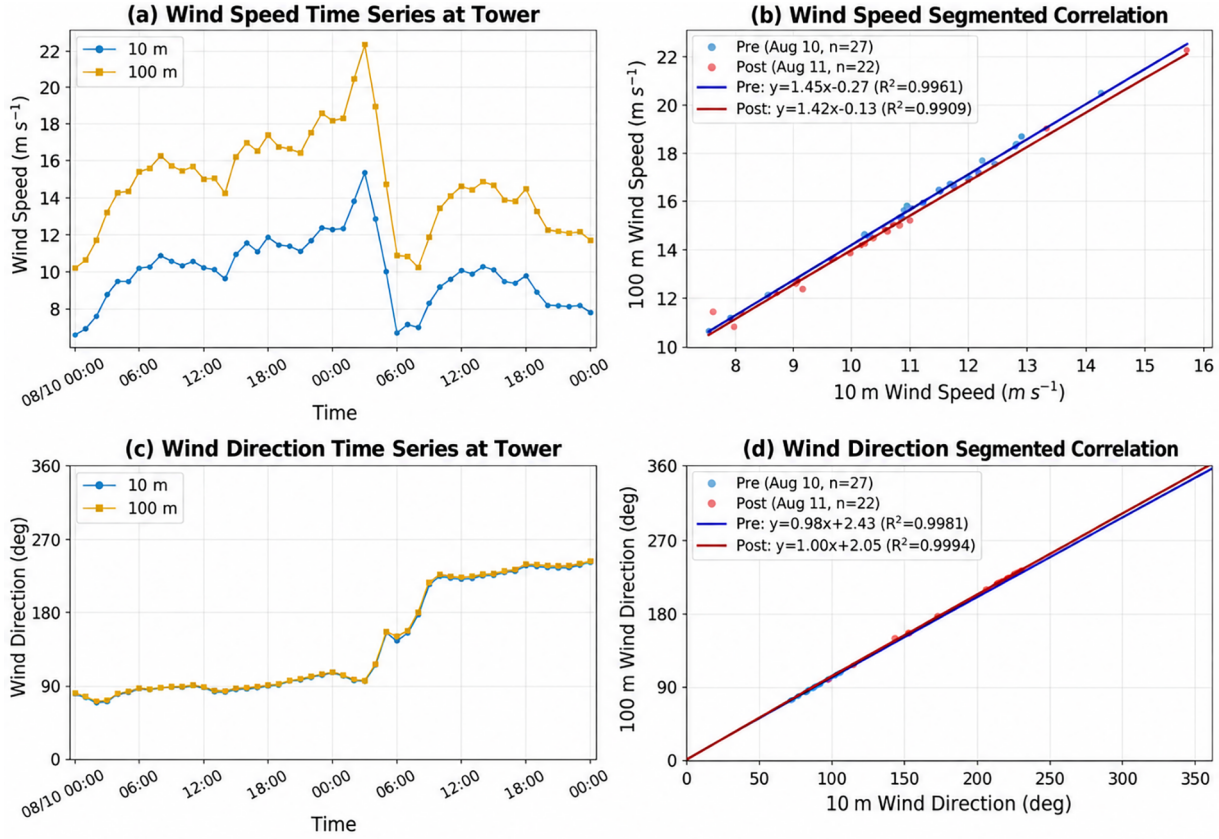


Figure 6: 10 vs. 100 m wind correlation at tower (120.7° E, 33.3° N). (**a**) Wind speed time series at tower, (**b**) wind speed segmented correlation, (**c**) wind direction time series at tower, (**d**) wind direction segmented correlation.

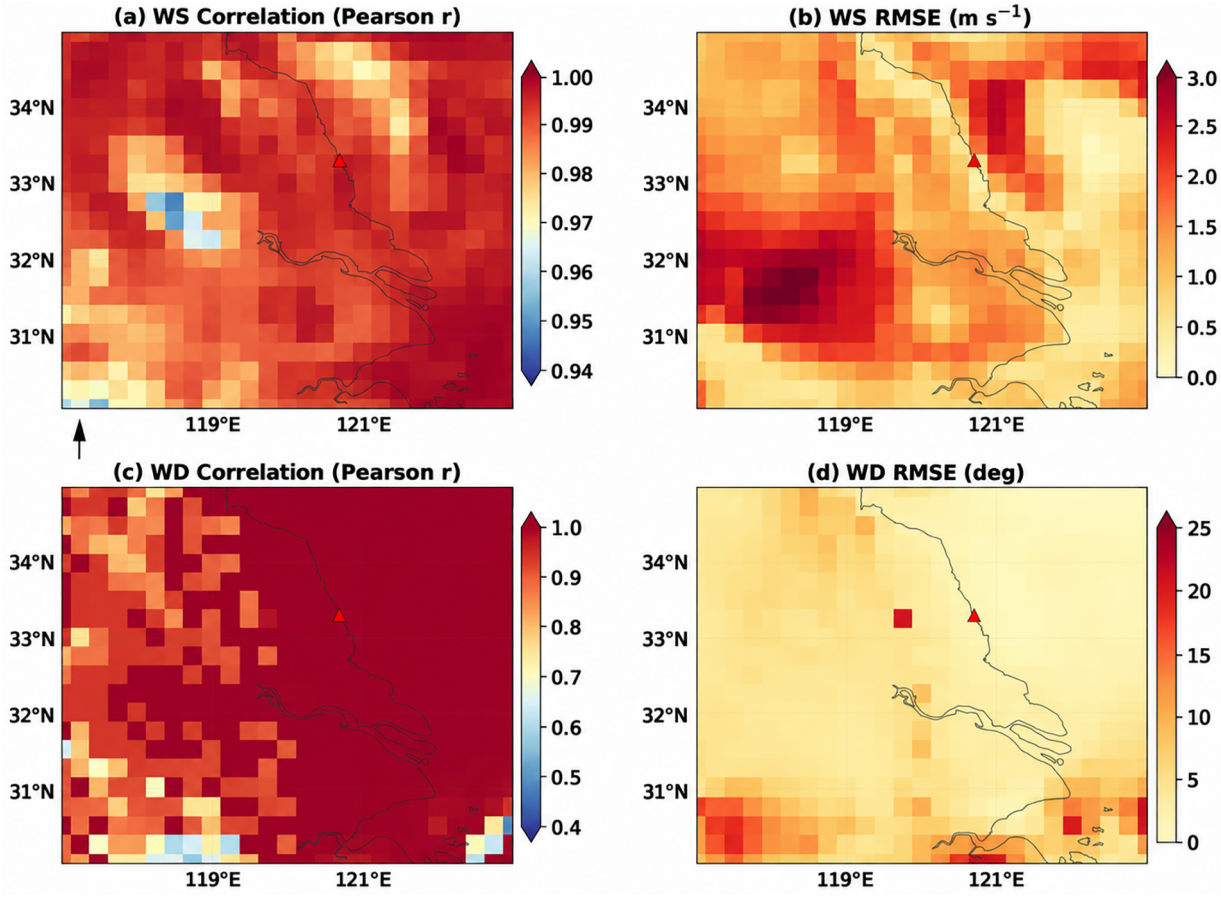


Figure 7: Spatial distribution of 10 vs. 100 m wind correlation during Typhoon Lekima. (**a**) WS correlation (Pearson r), (**b**) WS RMSE (m/s), (**c**) WD correlation (Pearson r), (**d**) WD rmse (deg).

4.4 Spatial Analysis of the Impacts of Mesoscale Meteorological Characteristics on Wind Fields

4.4.1 Influence of Air Temperature on Wind Fields

As shown in Fig. 8, the spatial distribution of 2 m air temperature overlaid with 10 m wind vectors is presented during the period from 04:00 on 10 August to 00:00 on 12 August 2019. Fig. 8 illustrates the spatial distribution of 850 hPa air temperature combined with 100 m wind vectors. A comparison between Figs. 8 and 9 reveals systematic vertical differences in the thermal–dynamic responses of the wind field during the passage of Typhoon Lekima.

Before the arrival of the typhoon center at the observation tower (04:00–20:00 on August 10), the near-surface isotherms at 2 m exhibited a relatively organized structure with weak spatial variability, with a standard deviation of only 0.46°C. Meanwhile, the wind vectors were mainly concentrated in the southeast quadrant, with a standard deviation of wind direction (WD10) of 5.6°. The high spatial consistency between the temperature field and wind vector distribution indicates that the atmospheric boundary layer remained in a coupled state dominated by systematic baroclinic forcing from the outer region of the typhoon circulation.

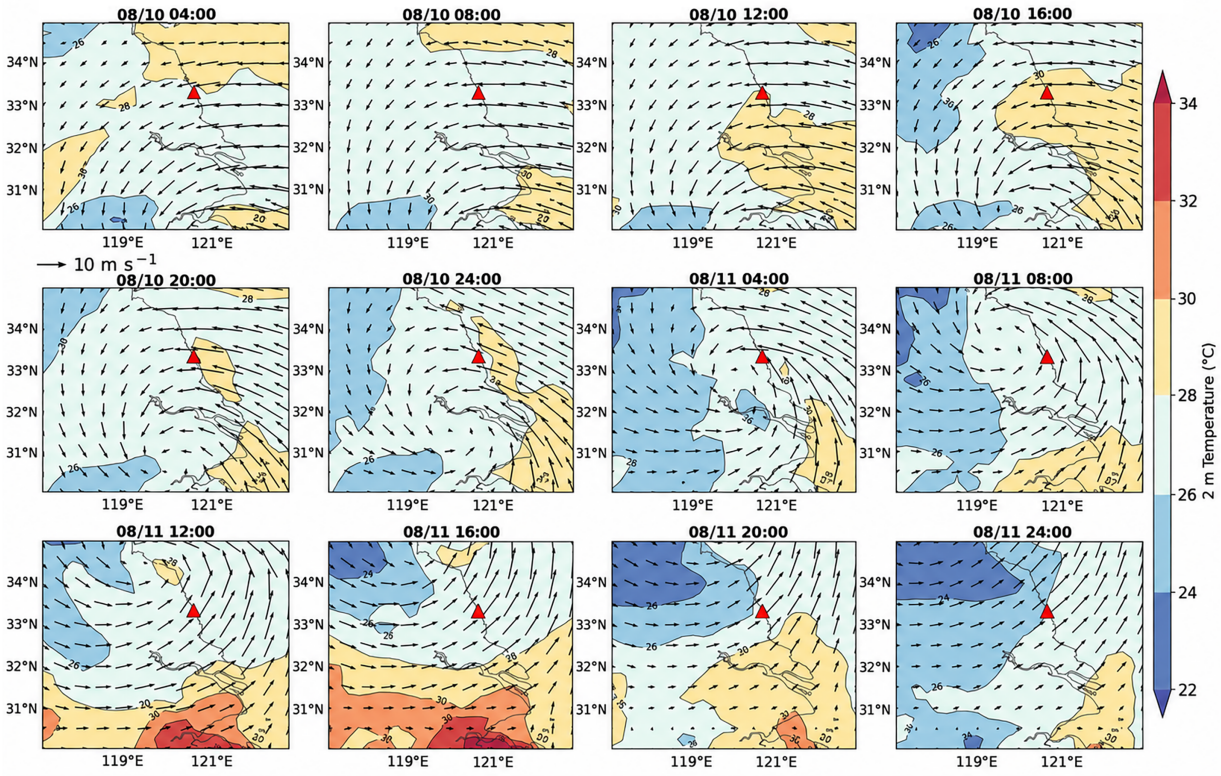


Figure 8: Spatiotemporal evolution of 2 m air temperature fields and 10 m wind vectors at 4-h intervals during the passage of Typhoon Lekima (04:00 10 August–24:00 11 August 2019). The red triangle represents the location of the meteorological tower.

After the passage of the typhoon eyewall (from August 11 onward), the near-surface temperature field became fragmented, with disrupted isotherms and enhanced local horizontal thermal gradients. Correspondingly, wind direction rapidly shifted from southeast to southwest within several hours, with the standard deviation increasing to 48.2°, while the temporal dispersion of wind speed expanded to nearly three times its pre-typhoon level. In contrast, the 850 hPa temperature field exhibited a relatively coherent warm-core structure before typhoon landfall, characterized by a closed high-temperature region corresponding to the near-surface warm zone, with a temperature standard deviation of 0.39°C. After the typhoon passage, this warm-core structure rapidly weakened, accompanied by a temperature decrease of approximately 4°C.

The distinct responses between different atmospheric layers can be attributed to the vertical modulation of surface friction and thermal forcing. The 10 m wind field is located within the roughness sublayer, where surface drag exerts an inertial smoothing effect on high-frequency wind fluctuations associated with cold-pool outflows and gust fronts. In contrast, the 70–100 m layer extends beyond the dominant frictional constraint zone and responds more directly to buoyancy-driven fluctuations generated by horizontal thermal contrasts between cold outflows and surrounding warm air masses. Consequently, high-frequency disturbances are better preserved at these elevated levels, leading to more frequent structural transitions and stronger non-stationary characteristics in wind speed and wind direction sequences [15].

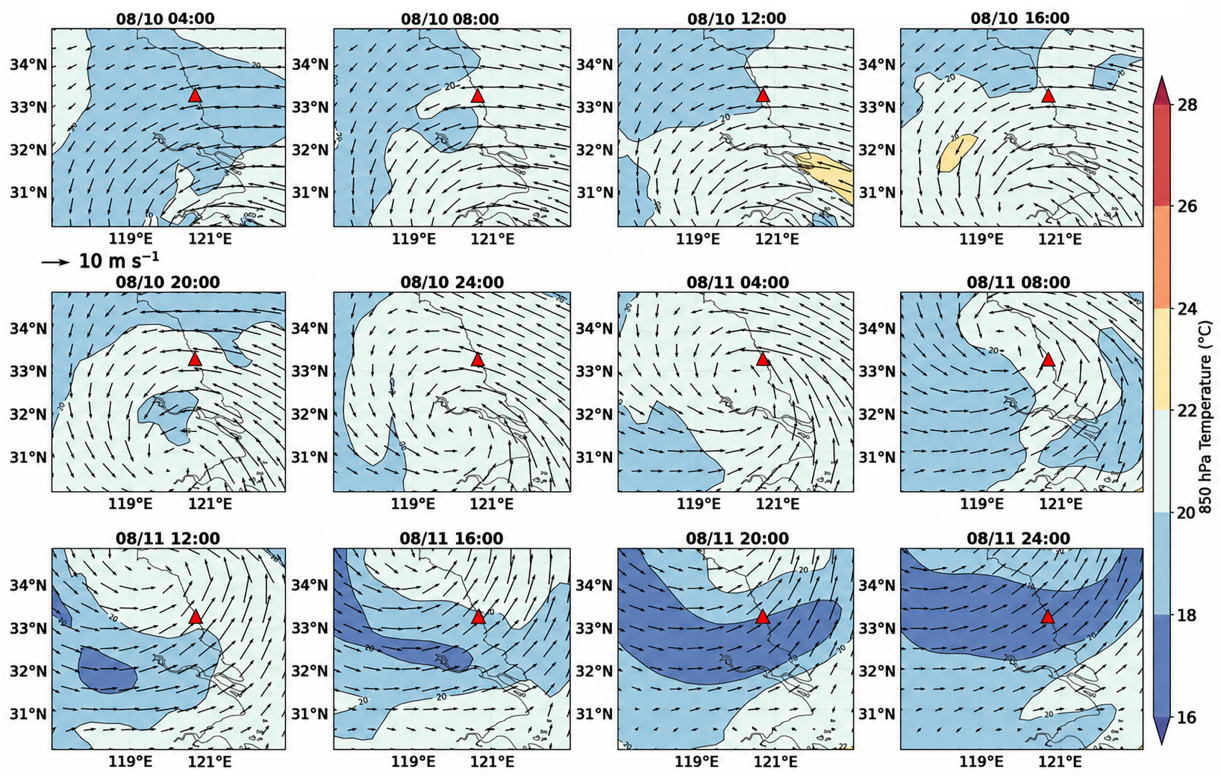


Figure 9: Spatiotemporal evolution of 850 hPa air temperature fields and 100 m wind vectors at 4-h intervals during the passage of Typhoon Lekima (04:00 10 August–24:00 11 August 2019). The red triangle represents the location of the meteorological tower.

Before the passage of the typhoon center, wind field variability was primarily controlled by the persistent mechanical forcing associated with the radial pressure gradient of the typhoon vortex. The relatively stable energy input resulted in strong vertical coupling within the boundary layer, allowing wind speed sequences to maintain pronounced inertial memory and long-range dependence. After the typhoon center passed, the thermal structure of the typhoon system rapidly weakened, and the dominant atmospheric forcing shifted from large-scale pressure-gradient forcing to multiple localized and transient thermal disturbances, including near-surface cold pools induced by rainfall evaporation cooling and convective downdrafts [16]. These processes are short-lived and spatially discontinuous, making it difficult to sustain persistent correlations within wind speed sequences. As a result, long-range dependence gradually degraded into short-term fluctuations, accompanied by enhanced non-stationarity and reduced temporal autocorrelation of the wind field.

4.4.2 Influence of Pressure Fields on Wind Fields

As shown in Fig. 10, the spatial distribution of near-surface pressure overlaid with 10 m wind vectors is presented, while Fig. 11 illustrates the spatial distribution of mean sea level pressure (MSLP) combined with 100 m wind vectors. The results indicate that the pressure field at the meteorological tower experienced the complete evolution process associated with the passage of Typhoon Lekima.

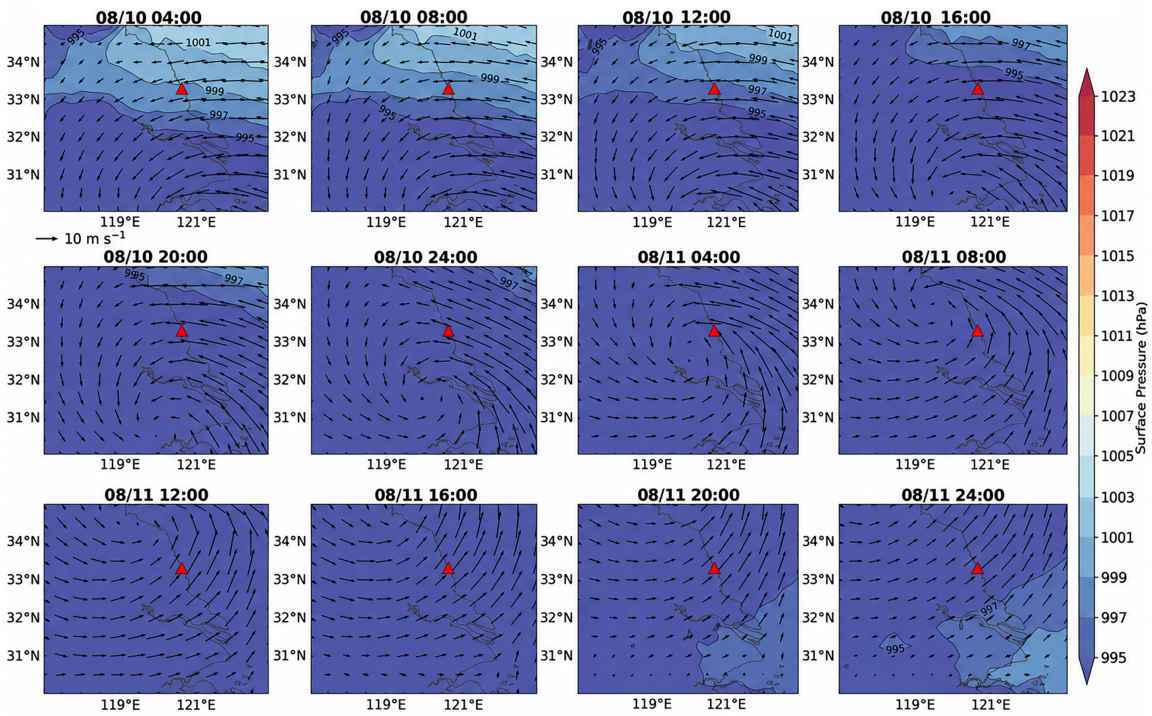


Figure 10: Spatiotemporal evolution of near-surface pressure fields and 10 m wind vectors at 4-h intervals during the passage of Typhoon Lekima (04:00 10 August–24:00 11 August 2019). The red triangle indicates the location of the meteorological tower.

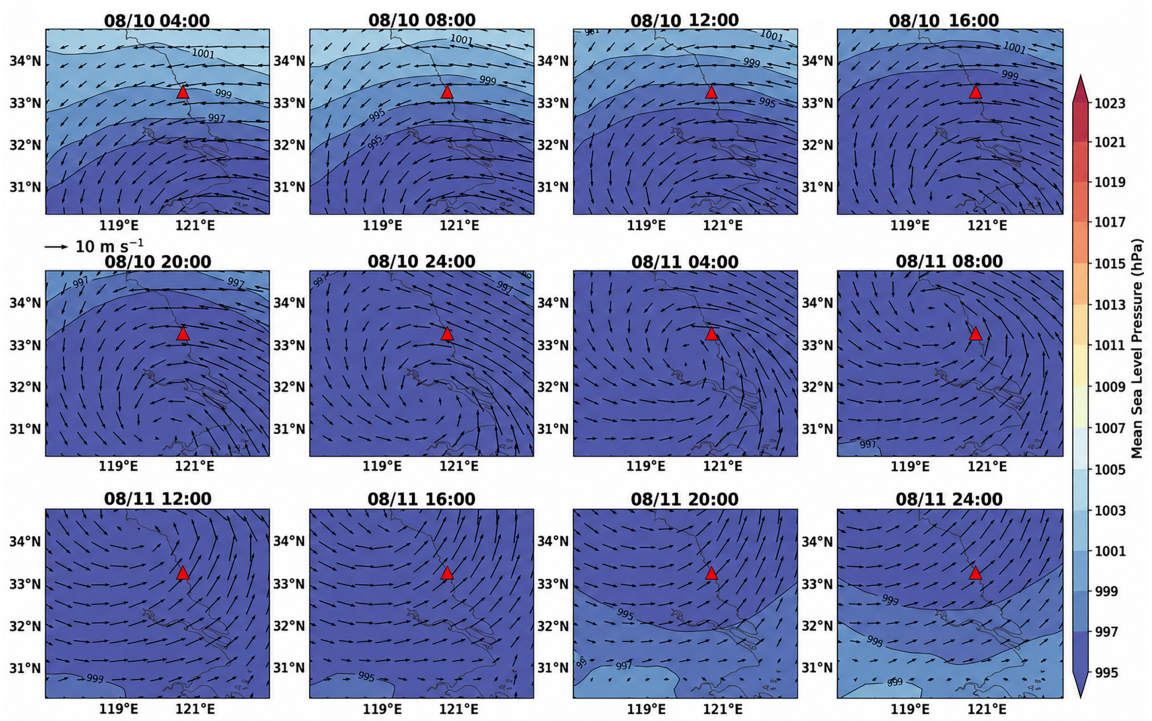


Figure 11: Spatiotemporal evolution of mean sea level pressure (MSLP) fields and 100 m wind vectors at 4-h intervals during the passage of Typhoon Lekima (04:00 10 August–24:00 11 August 2019). The red triangle indicates the location of the meteorological tower.

Before the arrival of the typhoon center, surface pressure continuously decreased from 999 to 990 hPa, and the spatial distribution of pressure gradients exhibited a consistent directional pattern, with a mean gradient magnitude of 3.58 hPa/°. The wind vectors at both 10 and 100 m maintained a highly consistent southeasterly flow, with standard deviations of wind direction (WD10 and WD100) of approximately 5.6°. Wind speeds gradually increased, and the spatial configuration between the wind field and pressure field was consistent with the gradient wind balance relationship [17].

During the passage of the typhoon center (early morning on August 11), the pressure reached its minimum value of 981.5 hPa, while the 100 m wind speed rapidly increased to 22.3 m s^{-1}. Meanwhile, the wind direction abruptly shifted from southeast to southwest. After the typhoon passage, pressure gradually recovered to 993 hPa; however, the spatial organization of pressure gradients became increasingly irregular. The mean pressure gradient increased to 4.44 hPa/°, while the dispersion of 10 m wind speed increased from 0.73 to 1.95 m s^{-1}, and that of 100 m wind speed increased from 1.07 to 2.84 m s^{-1}. Meanwhile, the standard deviations of wind direction at both heights rapidly increased from approximately 5.6° to 48.2°.

It is noteworthy that near-surface pressure and mean sea level pressure exhibited almost identical values around the observation site in Figs. 10 and 11, with a difference of less than 0.1 hPa. However, the 100 m wind speed remained approximately 1.4 times higher than the 10 m wind speed throughout the period, consistent with the logarithmic wind profile relationship. Meanwhile, wind directions at 10 and 100 m were almost completely synchronized, with a directional difference of less than 1°, indicating no significant directional wind shear during the typhoon event. A positive relationship was observed between pressure gradient magnitude and wind speed, with correlation coefficients of 0.57 between near-surface pressure gradients and 10 m wind speed, and 0.50 between MSLP gradients and 100 m wind speed. These results demonstrate that pressure-gradient force served as the dominant dynamic driver of wind speed variability.

The influence of surface pressure on the 10 m wind field was characterized by the combined effects of pressure-gradient forcing and surface frictional modulation. During the pre-typhoon stage, the persistent radial pressure gradient associated with the outer circulation of Typhoon Lekima provided a stable horizontal acceleration source for the atmospheric boundary layer. Consequently, the 10 m wind speed increased gradually, with a mean value of 11.4 m s^{-1} and a standard deviation of only 0.73 m s^{-1}. The wind vectors exhibited a nearly constant deflection angle relative to the isobars, broadly consistent with the classical behavior of winds within the lower Ekman layer.

After the typhoon passage, although the filling of the typhoon core caused the disappearance of the extreme low-pressure center, the mean local pressure gradient even increased by approximately 24%. However, the directional consistency of the pressure gradient was substantially disrupted. In the spatial distribution maps, the smooth curved isobaric structures before the typhoon passage transformed into fragmented and intersecting patterns, leading to frequent spatial changes in the direction of pressure-gradient force vectors. Under these conditions, This was accompanied by a substantial deterioration of wind speed and wind direction stability, with the standard deviation of WD10 increasing from 5.6° to 48.2°.

The influence of MSLP on the 100 m wind field followed a similar physical mechanism. However, because the 100 m layer extends beyond the direct influence of the surface roughness sublayer, the wind field at this height exhibited a higher sensitivity to variations in pressure-gradient forcing. The absolute fluctuation magnitude of WS100 (σ = 2.84 m s^{-1}) was significantly larger than that of WS10 (σ = 1.95 m s^{-1}), indicating stronger high-level wind responses under unstable pressure-gradient conditions.

The evolution of wind speed and wind direction observed by the meteorological tower clearly captured this coupling process. One hour before the minimum pressure occurred (03:00 on August 11), WS10 and WS100 simultaneously reached their maximum values (15.7 and 22.3 m s^{-1}, respectively). At the time of

minimum pressure (05:00), the wind direction rapidly shifted from southeast to southwest. Subsequently, as the spatial organization of the pressure field weakened, both wind speed and wind direction entered a state of high-frequency fluctuation. This transition represents the shift of atmospheric forcing from coherent large-scale pressure-gradient control to fragmented localized forcing, which was directly captured by the single-point observations from the meteorological tower [18].

5 Discuss

5.1 The BFAST Method Is Applied to the Non-Stationary Characteristics of Wind Speed

As a new time series change detection method, the BFAST method is more widely used in the feature extraction of climate, surface and hydrological changes [19]. BFAST decomposes a time series into trend, seasonal, and residual components and iteratively detects one or more structural change points (breakpoints) by segmenting the trend component, thereby avoiding the stationarity assumption that limits conventional linear methods. Compared with approaches such as EMD, whose results can be distorted by noise when all extreme points are retained [9], BFAST explicitly separates the periodic component and provides robust estimates of both the timing and the magnitude of abrupt changes. These advantages make BFAST particularly well suited to capturing the non-stationary behavior of the wind field during typhoon events, in which wind speed undergoes sudden acceleration and deceleration as the storm approaches and passes.

BFAST is applied to detect the non-stationary characteristics of wind speed. The analysis shows that the detected breakpoints are closely synchronized with the typhoon passage: at the tower site, the breakpoint occurs at 43 h after 00:00 UTC on 8 August at both heights, coinciding with the period of most rapid wind speed change during the approach of Typhoon Lekima, and the breakpoint magnitude (+1.34 m/s at 10 m and +2.20 m/s at 100 m) quantifies the abruptness of the structural transition. This confirms that BFAST is capable of capturing the timing and trength of the typhoon-induced regime shift in the wind speed time series.

Moreover, the 100% detection rate across the domain and the spatial distribution of breakpoints (earlier in the southeastern quadrant and progressively later toward the northwest) indicate that the regime shift is systematic rather than a local artifact, and that the structural transition propagates spatially along the typhoon track.

It should be noted that this study employed ERA5 reanalysis data with relatively coarse spatial (0.25°) and temporal (1 h) resolution, which may affect the accuracy of breakpoint detection and persistence characterization [20]. Because ERA5 represents the grid-averaged wind field rather than point-scale measurements, sharp wind speed fluctuations at the turbine scale may be smoothed, potentially leading to a slight underestimation of breakpoint magnitudes and a lower sensitivity to very short-lived structural changes [21]. Future work could combine BFAST with higher-resolution observations (e.g., tower measurements, lidar, or mesoscale model output) and with complementary indicators such as the Hurst exponent to further verify the robustness of the detected breakpoints and to better characterize the persistence of the wind field.

5.2 Analysis of Factors Influencing Wind Field Evolution Characteristics

The Hurst exponents show that the wind speed and wind direction series are strongly persistent (long-range dependent) during the typhoon, and the 100 m wind speed is slightly more persistent than at the other heights (Hurst = 0.991 at 100 m and 0.988 at 10 m). Hu Bo examined the factors behind coastal typhoon gust factors and found that mean wind speed and the gust factor both grow with typhoon intensity, which favors the occurrence of extreme winds; station terrain and height, the distance and orientation of the typhoon relative to the station, and the typhoon circulation together control how wind speed and the gust factor change [22]. Chen et al. studied the wind characteristics over different underlying surfaces during Typhoon

Soudelor and found that the strong non-stationarity of wind speed and wind direction depends mainly on the distance from the station to the typhoon center—the closer the station, the larger the changes—and that the underlying surface also affects the wind speed observed at the station [23]. The stronger persistence of the 100 m wind speed series reflects the combined influence of the typhoon circulation and the underlying surface roughness [24].

Geographic heterogeneity. The spatial grid analysis revealed systematic geographic heterogeneity in the 10–100 m wind coupling. Over the open ocean, wind speed correlation coefficients exceeded 0.99, whereas nearshore and coastal land areas exhibited reduced values (~0.95). This spatial gradient reflects the land–sea contrast in surface roughness length (z_0), which transitions from $O(10^{-4})$ m over the ocean to $O(10^{-1}–10^{0})$ m over heterogeneous terrain, thereby enhancing mechanical turbulence in the roughness sublayer at 10 m that is absent at 100 m [25]. Wind direction correlation degradation, in contrast, was not geographically uniform but spatially confined to the typhoon inner-core region (minimum r = 0.49, RMSE up to 20°), where supergradient winds and strong horizontal shear generate differential Ekman veering between the two heights [26,27]. This indicates that directional decoupling is a storm-structure-dependent phenomenon rather than a ubiquitous boundary layer property. It should be noted, however, that the assumption of the 100 m level remaining within the inertial sublayer (surface layer) is most valid under near-neutral, mechanically driven conditions before the typhoon; as the boundary layer deepens and destabilizes during and after the passage of the storm center, the 100 m level may intermittently approach or exceed the top of the surface layer, which would modulate the vertical coupling between the two heights.

Spatial environmental response. The segmented temporal analysis demonstrated that the boundary layer wind field responded distinctly to the evolving meteorological environment across the typhoon passage. Prior to center arrival, the organized large-scale pressure gradient (3.58 hPa/deg) maintained strong vertical thermal coupling (r = 0.57 between 2 m and 850 hPa temperatures) and well-constrained wind direction sequences (σ = 5.6°). Following center passage, the collapse of systematic pressure forcing coincided with a 43% increase in 2 m spatial temperature gradients, driven by precipitation-induced cold pools and differential surface heating. This the spatial fragmentation (heterogeneity) of the thermal field shifted the dominant forcing mechanism of the boundary layer from mechanical shear to buoyancy-driven turbulence, increasing 10 m wind speed variance nearly threefold (σ from 0.73 to 1.95 m/s) and slightly reducing wind speed correlation (R^2 from 0.996 to 0.991). The 100 m wind field, situated near the top of the Ekman layer with reduced frictional anchoring, responded more sensitively to these buoyancy perturbations, consistent with the elevated RMSE observed within the inner-core region [28]. These results indicate that atmospheric stability changed substantially across the typhoon passage: the pre-typhoon boundary layer was near-neutral and mechanically well coupled, whereas the post-typhoon boundary layer became less stable owing to cold-pool outflows and differential surface heating. Such stability changes, together with variations in boundary layer depth, imply that the 100 m level cannot always be assumed to lie within the inertial sublayer. More generally, surface friction (roughness-dependent mechanical drag) and thermal forcing (stability- and buoyancy-related) jointly modulate the coupling between the 10 and 100 m wind fields, which accounts for the generally stable yet spatially and temporally variable wind speed ratio and correlation observed in this study.

Collectively, the geographic heterogeneity in wind coupling arises from the superposition of surface roughness modulation near coastlines and storm-structure-dependent directional shear within the convective core, while the spatial environmental response reflects the fundamental transition from a mechanically driven, well-coupled boundary layer to a thermally fragmented, locally forced regime in the post-typhoon environment.

5.3 The Influence of Wind Speed and Wind Direction Non-Stationarity on Wind Turbines

The effective, long-term stable operation of wind turbines is essential for wind power enterprises to achieve long-term benefits and sustainable development. Chen Qiuyang noted that the siting of wind farms in China's offshore and coastal areas, the turbine design, and the occurrence and development of tropical cyclones in the Northwest Pacific are factors that must be considered during wind farm operation. Typhoons also place higher demands on the control capabilities of wind turbines, such as pitch control and yaw [23]. Chen et al., studying the characteristics of typhoon peripheral winds in northern Jiangsu and their impact on wind turbine selection, found that although the 10-min mean wind speed of the peripheral wind did not exceed the turbine cut-out speed, the turbulence intensity in the gale section exceeded the design level and would increase impeller fatigue and shorten blade service life [29]. Therefore, wind farm planning and siting must account for the risk of sudden wind-parameter changes induced by typhoons together with the surrounding terrain. Typhoon-resistant turbine design should consider the load capacity of components under extreme winds and the execution of control strategies. During operation and maintenance, typhoon early warning and emergency response should be actively carried out.

6 Conclusion

This study systematically investigated the non-stationary evolution of the 10 and 100 m wind speed fields during Typhoon Lekima (2019) using ERA5 reanalysis data, employing a combined approach of BFAST breakpoint detection and Hurst exponent analysis. The influence of meteorological factors on the non-stationarity of the wind field was further examined. The principal findings are summarized as follows:

(1) BFAST single-breakpoint detection identified structural change points at all 525 grid cells, yielding a 100% detection rate. The spatial distribution of breakpoint timing exhibited a progressive delay along the storm track (median 26 h at 10 m, 33 h at 100 m), with positive breakpoint magnitudes in the northeastern sector and negative magnitudes in the southwestern sector, reflecting the asymmetric wind field evolution characteristic of a translating tropical cyclone. Segmented fitting at the tower site revealed synchronous breakpoints at 43 h for both levels, with pre-break positive trends transitioning to post-break negative trends and breakpoint magnitudes of +1.34 m/s (10 m) and +2.20 m/s (100 m), indicating a stronger response at the upper level.

(2) Wind speed and wind direction Hurst exponents exhibited divergent memory dynamics. Following typhoon center passage, the tower-site wind speed Hurst exponent decreased substantially from approximately 1.04 to 0.84, indicating that turbulent kinetic energy injection disrupted the long-range memory of wind speed sequences. In contrast, the directional Hurst exponent increased modestly from approximately 0.88 to 0.91, demonstrating that the post-storm wind field settled into a stable southwesterly flow with enhanced directional persistence. This scalar-decay–directional-enhancement memory dichotomy was corroborated by the domain-wide Hurst spatial distributions.

(3) The attenuation of long-range dependence observed in post-typhoon wind speed sequences is primarily associated with the disruption of large-scale pressure-gradient coherence, which shifts the dominant boundary-layer forcing from organized baroclinic forcing to localized stochastic thermal perturbations.

In this paper, the change characteristics and influencing factors of wind speed and direction of wind tower are studied, which provides methods and theoretical support for the study of short-term wind speed when typhoon passes through, The proposed framework improves the understanding of coastal atmospheric spatial dynamics under typhoon conditions and provides useful geospatial evidence for coastal hazard assessment, environmental monitoring, offshore wind-resource evaluation, and coastal planning.

Acknowledgement: We would like to thank China Southern Power Grid Company's New Power System Technology Project for providing funding for this research, and Jiangsu Haishanglongyuan Wind Power Co., Ltd., for providing wind speed and direction data. Thank you to everyone who contributed to the study.

Funding Statement: This work was supported by the New power system technology project of China Southern Power Grid Corporation (000000KK52210138), authors is Lingzi Wang.

Author Contributions: The authors confirm contribution to the paper as follows: study conception and design: Liyuan Deng; visualization: Jing Tan; data collection: Bing Bing; analysis and interpretation of results: Aodi Fu; draft manuscript preparation: Linzi Wang, Haibo Shen and Huijun Wu. All authors reviewed and approved the final version of the manuscript.

Availability of Data and Materials: The datasets used or analysed during the current study are available from the corresponding author on reasonable request.

Ethics Approval: Not applicable.

Conflicts of Interest: The authors declare no conflicts of interest.

References

1. Jiang B, Ding J, Fang YZ. Off wind energy and wave energy resource valuation in Weizhou Island. Acta Energiae Solaris Sin. 2023;44(10):461–6. (In Chinese).
2. Eain W, Leephakpreeda T. A comprehensive approach to mechanical performance prediction of wind turbines considering key design factors via dimensional analysis and angular momentum conservation. Sci Rep. 2025;15(1):44985. doi:10.1038/s41598-025-29274-x.
3. Liu M, Liu K, Wang Z, Zhang C, Xie Z. Field measurement study on typhoon wind characteristics during strong wind periods. J Wind Eng Ind Aerodyn. 2025;265(11):106158. doi:10.1016/j.jweia.2025.106158.
4. Dai Y, Zhang M, Jiang F, Zhang J, Liu M, Hu W. Wind speed multi-step prediction based on the comparison of wind characteristics and error correction: focusing on periodic thermally-developed winds. Eng Appl Artif Intell. 2024;136:108924. doi:10.1016/j.engappai.2024.108924.
5. Chen X, Zuo C, Huang A, Wang Z, Song Z, Li Q, et al. Spatiotemporal responses of water level and wave height under multi-source wind-field forcing: a case study of Typhoon in-fa. Stoch Environ Res Risk Assess. 2026;40(7):179. doi:10.1007/s00477-026-03311-1.
6. Fu J, Yang L, Zhen X. Research and improvement methods for EMD on the basis of statistical models. Circuits Syst Signal Process. 2025;44(9):6606–21. doi:10.1007/s00034-025-03075-z.
7. Xulu S, Phungula PT, Mbatha N, Moyo I. Multi-year mapping of disturbance and reclamation patterns over Tronox's Hillendale Mine, South Africa with DBEST and google earth engine. Land. 2021;10(7):760. doi:10.3390/land10070760.
8. Chen C, Meng D. Analysis of variation of wind speed at low-altitude in Wuhan from 1958 to 2013. Resour Environ Yangtze Basin. 2015;24(S1):30–7. (In Chinese).
9. Huang J, Yu H, Guan X, Wang G, Guo R. Accelerated dryland expansion under climate change. Nature Clim Change. 2016;6(2):166–71. doi:10.1038/nclimate2837.
10. Verbesselt J, Hyndman R, Newnham G, Culvenor D. Detecting trend and seasonal changes in satellite image time series. Remote Sens Environ. 2010;114(1):106–15. doi:10.1016/j.rse.2009.08.014.
11. He B, Chang J, Wang Y, Wang Y, Zhou S, Chen C. Spatio-temporal evolution and non-stationary characteristics of meteorological drought in inland arid areas. Ecol Indic. 2021;126(6):107644. doi:10.1016/j.ecolind.2021.107644.
12. Ambach D, Schmid W. Periodic and long range dependent models for high frequency wind speed data. Energy. 2015;82(7):277–93. doi:10.1016/j.energy.2015.01.038.
13. Emeksiz C, Tan M. Multi-step wind speed forecasting and Hurst analysis using novel hybrid secondary decomposition approach. Energy. 2022;238(4):121764. doi:10.1016/j.energy.2021.121764.

14. Xu ZF, Zou JH, Li C. R/S analysis on Hurst exponent of wind speed time series. J Chin Soc Power Eng. 2019;654:850–62. (In Chinese).
15. Snaiki R, Wu T. Modeling tropical cyclone boundary layer: height-resolving pressure and wind fields. J Wind Eng Ind Aerodyn. 2017;170(10):18–27. doi:10.1016/j.jweia.2017.08.005.
16. Wang H, Wang Y. The role of diabatic heating/cooling in outer rainbands in the secondary eyewall formation and evolution in a numerically simulated tropical cyclone. Atmos Res. 2024;312(2):107730. doi:10.1016/j.atmosres.2024.107730.
17. Ahern K, Hart RE, Bourassa MA. Asymmetric hurricane boundary layer structure during storm decay. Part II: secondary eyewall formation. Mon Weather Rev. 2022;150(8):1915–36. doi:10.1175/mwr-d-21-0247.1.
18. Webster PJ, Holland GJ, Curry JA, Chang HR. Changes in tropical cyclone number, duration, and intensity in a warming environment. Science. 2005;309(5742):1844–6. doi:10.1126/science.1116448.
19. DeVries B, Verbesselt J, Kooistra L, Herold M. Robust monitoring of small-scale forest disturbances in a tropical montane forest using Landsat time series. Remote Sens Environ. 2015;161:107–21. doi:10.1016/j.rse.2015.02.012.
20. Ahmed KT, Baul S, Fu Y, Zhang W. Attention-based multi-modal missing value imputation for time series data with high missing rate. In: Proceedings of the 2023 SIAM International Conference on Data Mining (SDM); 2023 Apr 27–29; Minneapolis, MN, USA. p. 469–77. doi:10.1137/1.9781611977653.ch53.
21. Marinšek A, Bajt G. Demystifying the use of ERA5-land and machine learning for wind power forecasting. IET Renew Power Gener. 2020;14(19):4159–68. doi:10.1049/iet-rpg.2020.0576.
22. Hu B. Analysis of gust factor associated with typhoons on Zhejiang Coast. J Tropocal Meteorol. 2017;33(6):841–9. (In Chinese).
23. Chen QY, Li YC, Du WA. Analysis of wind characteristics of different underlying surfaces during the influence of Typhoon Soudelor. Wind Energy. 2019;(4):80–5. (In Chinese).
24. Wang LJ, Deng FJ, Shi HY. Distribution characteristics and causes of gale wind in Zhejiang province affected by Typhoon "Lekima" (1909). Mar Forecast. 2020;37(6):83–95. (In Chinese).
25. Grube G, Talbot B, Grigolato S. Automated terrain roughness assessment using remotely sensed data. Int J For Eng. 2025;36(3):299–314. doi:10.1080/14942119.2025.2480009.
26. Kepert J. The dynamics of boundary layer jets within the tropical cyclone core. Part I: linear theory. J Atmos Sci. 2001;58(17):2469–84. doi:10.1175/1520-0469(2001)0582.0.co;2.
27. Montgomery MT, Smith RK. Recent developments in the fluid dynamics of tropical cyclones. Annu Rev Fluid Mech. 2017;49(1):541–74. doi:10.1146/annurev-fluid-010816-060022.
28. Zhang JA, Rogers RF, Nolan DS, Marks FD. On the characteristic height scales of the hurricane boundary layer. Mon Weather Rev. 2011;139(8):2523–35. doi:10.1175/mwr-d-10-05017.1.
29. Chen JJ, Zhang M, Gao ZQ. Study on wind characteristics of typhoon periphery in northern Jiangsu Province and its influence on wind turbine selection. Acta Energiae Solaris Sinca. 2022;43(3):411–8. (In Chinese).